

| | | | | | |
|---|--------------------|--------------------------------|-----------------------------------|---|---|
| REPORT DOCUMENTATION PAGE | | | | <i>Form Approved</i> OMB No. 0704-0188 | |
| The public reporting burden for this collection of information is estimated to average 1 hour per response, including the time for reviewing instructions, searching existing data sources, gathering and maintaining the data needed, and completing and reviewing the collection of information. Send comments regarding this burden estimate or any other aspect of this collection of information, including suggestions for reducing the burden, to Department of Defense, Washington Headquarters Services, Directorate for Information Operations and Reports (0704-0188), 1215 Jefferson Davis Highway, Suite 1204, Arlington, VA 22202-4302. Respondents should be aware that notwithstanding any other provision of law, no person shall be subject to any penalty for failing to comply with a collection of information if it does not display a currently valid OMB control number. PLEASE DO NOT RETURN YOUR FORM TO THE ABOVE ADDRESS. | | | | | |
| 1. REPORT DATE (DD-MM-YYYY) 22-12-2014 | | 2. REPORT TYPE Final | | 3. DATES COVERED (From - To) 17 Jan 2013 to 17 Jun 2014 | |
| 4. TITLE AND SUBTITLE Thermal nonequilibrium in hypersonic separated flow | | | | 5a. CONTRACT NUMBER FA2386-13-1-4013 | |
| | | | | 5b. GRANT NUMBER Grant AOARD-134013 | |
| | | | | 5c. PROGRAM ELEMENT NUMBER 61102F | |
| 6. AUTHOR(S) Dr. Sean O'Byrne | | | | 5d. PROJECT NUMBER | |
| | | | | 5e. TASK NUMBER | |
| | | | | 5f. WORK UNIT NUMBER | |
| 7. PERFORMING ORGANIZATION NAME(S) AND ADDRESS(ES) University of New South Wales Northcott Drive Campbell, ACT 2600 Australia | | | | 8. PERFORMING ORGANIZATION REPORT NUMBER N/A | |
| 9. SPONSORING/MONITORING AGENCY NAME(S) AND ADDRESS(ES) AOARD UNIT 45002 APO AP 96338-5002 | | | | 10. SPONSOR/MONITOR'S ACRONYM(S) AOARD | |
| | | | | 11. SPONSOR/MONITOR'S REPORT NUMBER(S) AOARD-134013 | |
| 12. DISTRIBUTION/AVAILABILITY STATEMENT Distribution Code A: Approved for public release, distribution is unlimited. | | | | | |
| 13. SUPPLEMENTARY NOTES | | | | | |
| 14. ABSTRACT This project investigates the application of two diagnostic methods for the investigation of hypersonic separated flow in thermal nonequilibrium. This is part of a larger, international collaborative program to compare state-of-the art measurements of the thermal state of the flowfield with the best available computational predictions of the flowfield. This report discusses resonantly enhanced shearing interferometry visualizations, using alkali metals as the resonant seed species. This visualization technique is tested for a low-density hypersonic separated flow around a 'tick'-shaped leading-edge separated flow. Results for flow visualizations are obtained using lithium metal and a broadband laser, lithium chloride salt with the same laser, and rubidium chloride salt with a single-mode laser source. The differences in repeatability and image contrast for these three resonantly enhanced techniques are discussed, and the establishment of the flow at a high-enthalpy condition produced in a shock tunnel is investigated using tunable diode laser absorption spectroscopy. The visualization comparison indicates that for the purposes of visualization, a broadband laser source using lithium metal provides the best sensitivity to density variations and the best compromise between resonant enhancement of refractivity and absorption of the laser light. The effects of included angle and leading edge radius are compared using the resonantly enhanced shearing interferometry, and compared to direct simulation Monte Carlo calculations. The diode laser measurements provided important information on flow duration and steadiness. | | | | | |
| 15. SUBJECT TERMS Hypersonic Flowfield Measurements, Laser Diagnostics of Gas Flow, Laser Induced Fluorescence | | | | | |
| 16. SECURITY CLASSIFICATION OF: | | | 17. LIMITATION OF ABSTRACT | 18. NUMBER OF PAGES | 19a. NAME OF RESPONSIBLE PERSON Ingrid J. Wysong, Ph.D. |
| a. REPORT | b. ABSTRACT | c. THIS PAGE | | | 19b. TELEPHONE NUMBER (Include area code) +81-42-511-2000 |
| U | U | U | SAR | 24 | |

Leading-Edge Separation in Thermal Nonequilibrium Hypersonic Flow Final Report for AOARD Grant 134013

S. O'Byrne, S.L. Gai, T. Kaseman, Y. Krishna, H. H. Kleine and A. Neely

*School of Engineering and Information Technology, University of New South Wales, Canberra, ACT, 2600,
Australia*

Abstract. This paper investigates the application of two diagnostic methods for the investigation of hypersonic separated flow in thermal nonequilibrium. This is part of a larger, international collaborative program to compare state-of-the art measurements of the thermal state of the flowfield with the best available computational predictions of the flowfield. This report discusses resonantly enhanced shearing interferometry visualizations, using alkali metals as the resonant seed species. This visualization technique is tested for a low-density hypersonic separated flow around a 'tick'-shaped leading-edge separated flow. Results for flow visualizations are obtained using lithium metal and a broadband laser, lithium chloride salt with the same laser, and rubidium chloride salt with a single-mode laser source. The differences in repeatability and image contrast for these three resonantly enhanced techniques are discussed, and the establishment of the flow at a high-enthalpy condition produced in a shock tunnel is investigated using tunable diode laser absorption spectroscopy. The visualization comparison indicates that for the purposes of visualization, a broadband laser source using lithium metal provides the best sensitivity to density variations and the best compromise between resonant enhancement of refractivity and absorption of the laser light. The effects of included angle and leading edge radius are compared using the resonantly enhanced shearing interferometry, and compared to direct simulation Monte Carlo calculations. The diode laser measurements provided important information on the duration and steadiness of the flow.

Keywords: hypersonic, separated flow, flow visualization, TDLAS

PACS: 47.32.Ff, 47.40.Ki

1. INTRODUCTION

Low-density flows present a challenge for experimentalists, because whatever physical mechanism is chosen for the investigation, those wishing to perform experiments have a problem of relatively small concentrations of molecules or atoms. This leads to a lack of signal in absolute terms or a lack of sensitivity to changes in signal. This is even the case for well established, standard visualization techniques like differential interferometry or schlieren visualization. The difficulties with low signal are enhanced in high-enthalpy flows, where there is competing signal due to emission from excited species and high temperatures that ensure still lower population fractions in individual internal energy states. This report outlines the development of two techniques for making measurements and performing visualizations in low-density hypersonic flows: resonantly enhanced shearing interferometry and tuneable diode laser absorption spectroscopy. These techniques have been deployed to investigate the behavior of a particular case in hypersonic leading-edge separation, which we describe here as a 'tick' configuration because of its resemblance to a tick or check mark.

The aim of the project is to apply new methods to determine the freestream conditions and the flow steadiness for this configuration. The project is part of a larger collaborative project involving the application of several measurement techniques to the problem, including planar laser-induced fluorescence (PLIF) of velocity and rotational temperature of nitric oxide and coherent anti-Stokes Raman scattering (CARS) point measurements of rotational and vibrational temperatures of molecular nitrogen and oxygen. By the application of all these methods to the leading-edge separated flow field, the agreement with state-of-the-art numerical simulations can be determined. Previous investigations of these flowfields

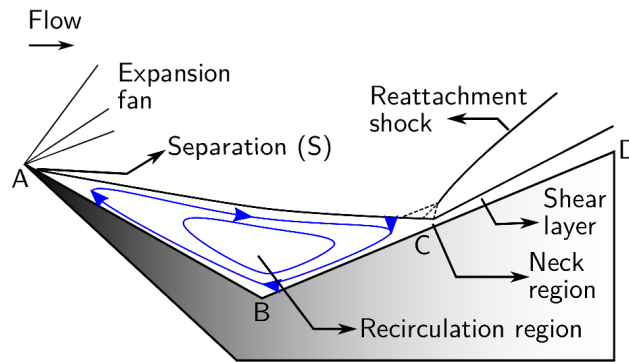


FIGURE 1. Schematic of 'tick' leading-edge separation configuration

1.1. Leading-Edge Separation

The leading-edge separation geometry is outlined in Fig. 1. This geometry was first suggested in one of the foundational papers on separation of compressible flows by Chapman [1], but has not been studied experimentally until quite recently, as other geometries such as rearward or forward-facing steps and compression corners have been more popular for experimental investigation. Reference [2] contains a current and thorough overview of these viscous interaction problems. One of the advantages of this configuration over the more commonly studied ones is that the flow separates very close to the leading edge, without developing a significant boundary layer thickness prior to separation. This is important, as the dominant analytical model for prediction of base pressure [3] assumes a zero-thickness boundary layer at the separation point. For the other separation geometries, which all tend to have an upstream region where the boundary layer can develop, this assumption may not always be valid.

The flow in Fig. 1 is characterized by an initial expansion of the flow downstream of the leading edge of the model. The compression on the downstream surface BD generates an adverse pressure gradient that causes the flow to separate somewhere on the surface AB . The shear layer extends from A to C , separating the outer inviscid flow from a recirculating viscous inner vortical flow. The size of the separated region ABC is determined by the balance of mass and momentum into and out of the vortex, and reaches a steady state under hypersonic laminar flow conditions.

Although a simple flowfield that is amenable to either computational or analytical investigation, the separated region has proved difficult to predict. This is particularly true as the Knudsen number of the flow, Kn , increases. At $Kn \geq 0.01$, molecules at the expansion surface AB begin to slip. This allows the molecules to overcome the pressure gradient for longer and results in a delay of the separation and a reduction in the size of the separated region. Figure 2, from Ref. [4], shows a direct comparison between Navier-Stokes (NS) and direct simulation Monte-Carlo (DSMC) simulations of the leading-edge separation. Because the DSMC models collisions between the sample molecules and the surface, the effect of slip is directly modeled, whereas in this case the NS code assumes a no-slip condition for the fluid at the wall surface. This leads to a significant difference in the prediction of the extent of the separation between the two codes, with the DSMC code predicting a separated region of smaller extent than the NS computation.

While it would be convenient to believe that the more physically realistic flow modeling of the DSMC gas-surface interaction would lead to a more accurate prediction of the size of the separated flow, previous comparisons with surface-measurement experiments performed on a separated double-cone geometry [5, 6] have indicated better agreement between NS solvers and experiment than for DSMC. Such important information can be obtained using a high-sensitivity flow visualization technique like the resonantly enhanced shearing interferometry method initially developed by Hruschka [7] in this report.

1.2. Increasing Sensitivity by Resonant Enhancement

For a schlieren system, the contrast in the image is given by ([8], [9])

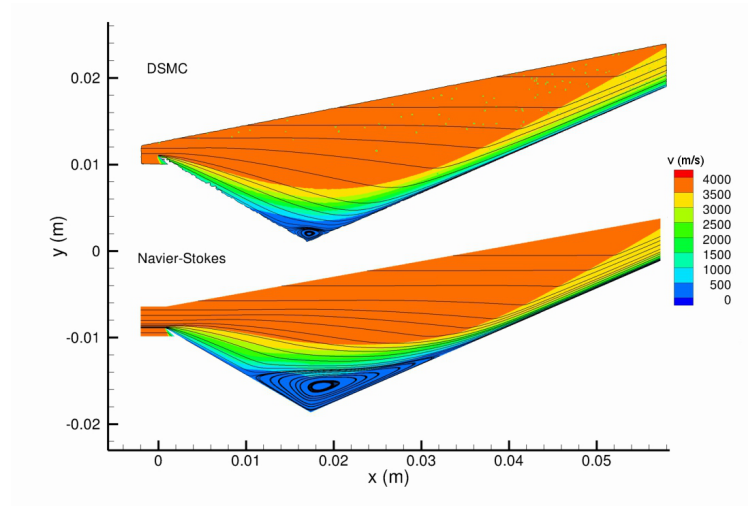


FIGURE 2. Comparison of DSMC and Navier-Stokes computations of leading-edge hypersonic separated flow, from [4]

$$\frac{I}{I_0} = \frac{f_2}{a} \int_{\xi_1}^{\xi_2} \frac{1}{n} \frac{\partial n}{\partial y} dz \quad (1)$$

where f_2 is the focal length of the schlieren focusing mirror or lens and a is the source size. The equivalent relation for the sensitivity a shearing interferometer is

$$\frac{I}{I_0} = 2 \cos^2 \left(\frac{f_2 \theta \pi}{\lambda} \int_{\xi_1}^{\xi_2} \frac{\partial n}{\partial y} dz \right). \quad (2)$$

It is clear that for both these cases, the absolute gradient in density is what controls the contrast, and for low-density flows the contrast can easily be below the limit of resolution of the optical imaging system. While it is clear from Eq. 1 that the sensitivity can be increased by either increasing the focal length of the schlieren lens or decreasing the source size, there are practical limitations to how well this can be done. Even if the sensitivity were able to be significantly increased using either of those two variables, the system would also be more sensitive to the density variations occurring outside the facility test section. It is for this reason that several investigators have considered resonant enhancement of the refractivity of gases at wavelengths near strong resonances of atomic species. When near a strong resonance there is a significant enhancement of the refractivity. According to the Kramers-Krönig relations [10], the refractive index n in the vicinity of a resonance is given by

$$n(\omega) = 1 + \frac{q_e^2}{2m_e \epsilon_0} \sum_i \frac{(\omega_{0i}^2 - \omega^2) f_i N_i}{(\omega_{0i}^2 - \omega^2)^2 + \gamma_i^2 \omega^2}, \quad (3)$$

where ω is the angular frequency of the transition, f_i and N_i are the oscillator strength of the transition and the number density of the absorbing species, γ_i is the collisional damping constant, q_e and m_e are the charge and mass of the electron and ϵ_0 is the permittivity of free space. Equation 3 holds for naturally broadened transitions. To be valid at the conditions used in a low-density hypersonic flow, the effect of Doppler broadening also needs to be taken into account. This is done by calculating the Doppler-shifted frequency $\omega_D = \omega_0(1 + v/c)$ for ω into eq. (3) and integrating over a two-dimensional Maxwell-Boltzmann velocity distribution given by

$$n_D(\omega) = 1 + \sqrt{\frac{m_M}{2\pi k_B T}} \int_{-\infty}^{\infty} (n(\omega_D) - 1) e^{-\frac{m_M v^2}{2k_B T}} dv \quad (4)$$

where m_M represents the atomic mass, k_B the Boltzmann constant, v the flow velocity, and T the temperature. The refractive index near the resonance will therefore deviate strongly from the non-resonant value of 1.001 in air when the

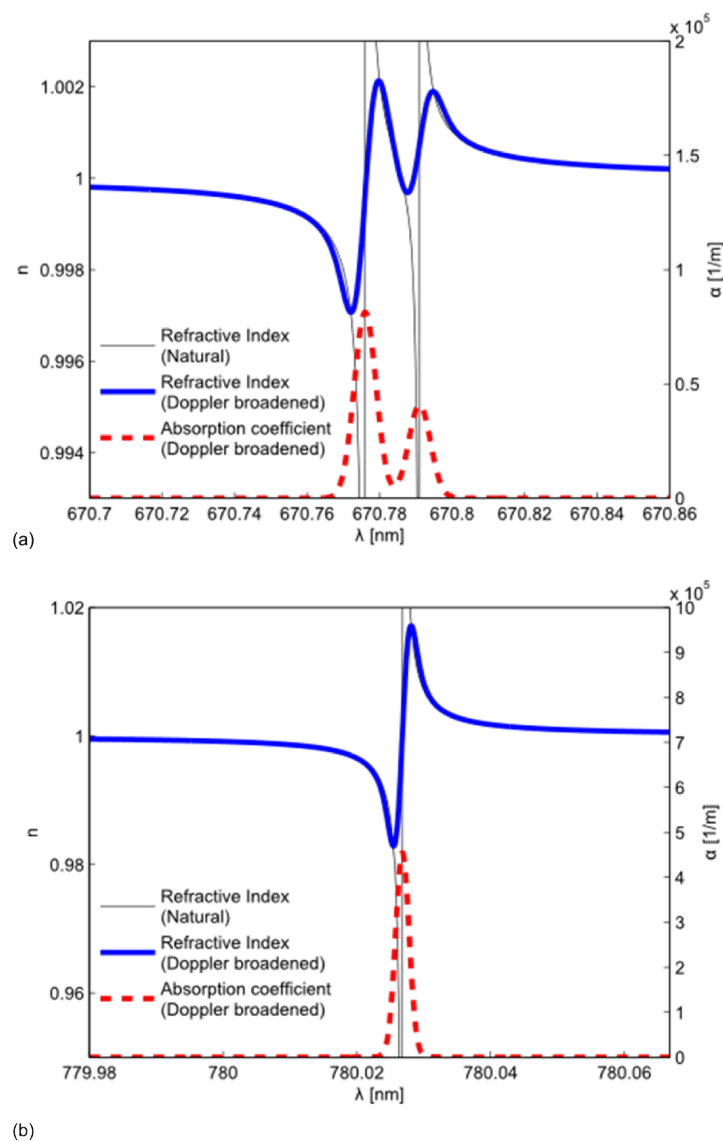


FIGURE 3. Resonantly enhanced refractivity and absorption coefficient in the vicinity of (a) the lithium *D* lines and (b) the rubidium *D2* line.

laser is tuned near a strong atomic absorption line. Figure 3(a), shows the refractive index and absorption coefficient α near the lithium *D* lines at 670.78 nm while Fig. 3(b) shows the same quantities for the rubidium *D2* line. In the case of rubidium the fine structure has not been accounted for directly, and the oscillator strengths have been lumped together, giving a slight overestimate of the maximum change in refractive index and absorption coefficient. Each of the curves was produced assuming a 0.5 % concentration of lithium at the Condition A nozzle exit conditions. Each of the plots in Fig. 3 contains three curves. The thin gray curve shows the refractive index for the naturally broadened transition calculated using Eq. 3, while the blue curve indicates the Doppler-broadened refractive index calculated using Eq. 4. The red curves indicate the absorption coefficient for the two transitions.

It is clear from the plots in Fig. 3 that there is significant enhancement of refractivity and very high levels of light attenuation in the vicinity of these strong transitions, even for low seed atom concentrations. It is also apparent when comparing the two plots that the rubidium line has greater refractivity enhancement and absorption coefficient than the Lithium lines. Most of this difference is caused by the higher molecular weight of the rubidium reducing the amount

of Doppler broadening of the transition, but some is due to the idealized oscillator strength model.

The above analysis shows that if one chooses to use a density-sensitive visualization technique using a light source operating at a wavelength close to a strong atomic line such as those for the alkali metals, the refractivity can be enhanced very significantly. The largest increases in refractive index will occur close to the transition, but at this point the absorbance will also be very high, and it becomes difficult to achieve sufficient signal because of attenuation of the light by the absorbing species. However, as Fig. 3 shows, the enhancement in refractivity decreases much more slowly away from resonance than does the absorbance. For this reason, it is possible to detune the light source several tens of picometers from the transition center and achieve significant enhancement of refractivity without attenuating the light source too much for flow visualization.

1.3. Previous Resonant Enhancement Studies

Leonard [11] was the first to investigate resonantly enhanced imaging, using a broadband spark source to produce sodium-enhanced white-light schlieren images of hypersonic projectile wakes. Blendstrup et al. [12] performed preliminary proof-of-concept measurements using a dye laser light source in a sodium seeded hot oven using a Mach-Zehnder interferometer to show the effect. Rasheed et al. [13] used near-resonant shadowgraphy with seeded sodium to investigate the flow around a toroidal ballute, the first free-piston shock tunnel investigation using this resonant enhancement technique. More recently Bishop [14] and McIntyre et al. [15] used sodium seeded into an expansion tube flow to perform quantitative holographic interferometry measurements using a dye laser as the excitation source.

Hruschka et al. [7] developed a system using resonantly enhanced shearing interferometry in seeded lithium metal, upon which the current investigation is based. The lithium was hammered into a foil which was placed at the entrance to the hypersonic nozzle in a free-piston shock tunnel. The high reservoir temperatures cause the metal to vaporize in the reservoir, and led to enhancement of an estimated factor of 100 times in the freestream of the facility. In contrast to previous studies, which had all used either a pulsed white light source or pulsed dye laser radiation to achieve still photographs, this technique used a continuous wave (CW) diode laser tuned near the lithium D lines shown in Fig. 3. The use of a CW laser allowed the technique to be combined with a high-frame-rate camera to produce video of the very rapid development of the wake flow.

While Hruschka et al. produced a technique that is very valuable for the time-resolved visualization of low-density hypersonic flow, two areas of potential improvement were subsequently identified, and these are explored in the present paper. The first is that the technique outlined by Hruschka et al. uses a multi-mode laser, which makes it very difficult to quantify the degree of resonant enhancement, as the laser behavior is not well characterized and the longitudinal mode structure of the laser light changes with time. The second potential area for improvement is that the lithium metal used in the method is highly reactive, and may react during the hammering of the material into a foil, or on exposure to liquid water. This study aims to investigate the effectiveness of two variants of the technique in a hypersonic separated flow: the use of a narrow-band, single-mode laser as the illumination source, and the use of lithium chloride and rubidium chloride salts as alternative seed species to the lithium metal used by Hruschka et al. [7]. In addition, as described in Sec. 1.2, the use of rubidium provides a higher degree of dispersion than for lithium, which has the potential to further enhance the refractivity of the low-density flow for visualization. This is an important consideration when dealing with the leading-edge separation geometry, because the lack of an initial bluff body means that the seed atom concentration is likely to be lower than that used in Hruschka et al. The discussion of the resonantly enhanced shearing interferometry (RESI) visualization in Sec. 3 will present an experimental comparison between these different RESI techniques for investigating the leading-edge separation problem.

2. COMPUTATIONAL INVESTIGATION

The experiments produced in this report were guided by DSMC computations of flow around the ‘tick’ configuration by Dr James Moss, and presented in Refs. [4] and [16]. Reference [4] outlined a comparison between DSMC and NS simulations of the flowfield at both continuum and transitional local Knudsen number conditions, and provided the initial motivation for this experimental work. Ref. [16] was a more detailed parametric study that investigated a number of parameters that were considered potentially important in determining the characteristics of the flow. Parameters investigated in that study included the effect of vibrational accommodation at the surface (found to be small, with a

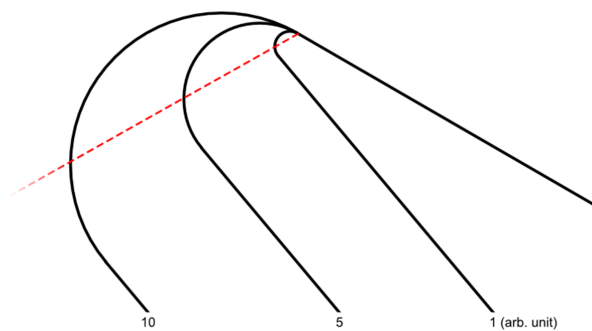


FIGURE 4. Variation in the bluntness of the model

maximum effect on heat flux of around 6 %), the effect of wall temperature, which was found to be significant but is challenging to test experimentally, and the effects of expansion surface length, leading-edge radius and bevel angle of the model's leading edge.

The part of Ref. [16] that will be summarized here because of its influence on the experimental results presented later is the investigation of the effects of leading-edge radius and the leading edge bevel angle (the included angle of the upstream portion of the model containing the expansion surface) on the flow features. The simulations were performed using G. A. Bird's DS2V code, an implementation of the direct simulation Monte Carlo method. The physical description of the method is described in detail in Bird's text [17], while the computational and operating details can be obtained from Ref. [18]. The detail of the computations used to obtain the solutions presented here can be found in Ref. [16]. The simulations were at a freestream condition that was the same in nearly all respects to Condition A, but with a lower freestream velocity of 3730 m/s compared with the experimental freestream velocity in Tab. 1. The difference was caused by following the conditions stated in Hruschka's thesis [19], in which the freestream velocity was mistakenly replaced with the incident shock speed into the test gas in the shock tube. While the results of the computations cannot therefore be directly compared to the results of the experiments presented in this report, it is reasonable to expect that the trends with leading edge radius and with leading edge bevel angle should be consistent for both freestream conditions. Computations with the correct freestream velocity are ongoing.

The computations were performed using 9.1 million simulated molecules and approximately 1 million collision cells, and while thermochemical non-equilibrium was assumed in a few individual cases, the parametric study was performed using a four-species non-reacting gas model, to save computational time. The ratio of the mean collision separation to the mean free path was maintained everywhere in the flowfield below unity, with the maximum value of 0.7 and a mean value of 0.13 throughout the flowfield.

Three leading edge bluntness values were chosen for the computational study: a 'sharp' mesh-limited case, a case with a $50\ \mu\text{m}$ radius and a case with a $100\ \mu\text{m}$ radius. The leading edge bluntness can be varied in a number of different ways. For this study it was decided to keep the same flat length of plate for each of the radius configurations. The method chosen for characterizing the effect of radius is summarized in Fig. 4. When the leading edge geometry is changed in this way, the total length of the model increases, and the stagnation point moves lower on the rounded part of the leading edge as the leading edge becomes more blunt, because the normal to the freestream direction moves to lower angles.

The DS2V code would not allow a model with a radius of less than $50\ \mu\text{m}$ to be generated, so a model with the experimentally measured radius could not be generated by DS2V for direct comparison with the sharpest of the experimental model configurations. The two bevel angles of 10° , 20.12° and 30° were investigated in the parametric study.

The effects of the leading edge radius, expansion surface length and bevel angle are summarized in Fig. 5 for the simulated flow conditions. This plot presents the change in the extent of the expansion region, Δs , with each of these parameters. Δs is defined as the wetted distance between the point of separation and the point of reattachment along the model surface. Separation and reattachment points are determined by where the computed surface shear stress changes sign along the model surface. Because the experimental mode changed over the course of the computations, there are older angles of 11.808° and 20.12° as well as more recent simulations of 10° , 20° and 30° on the plot. If a plot does not specifically mention a radius, then the solution is for a sharp leading edge.

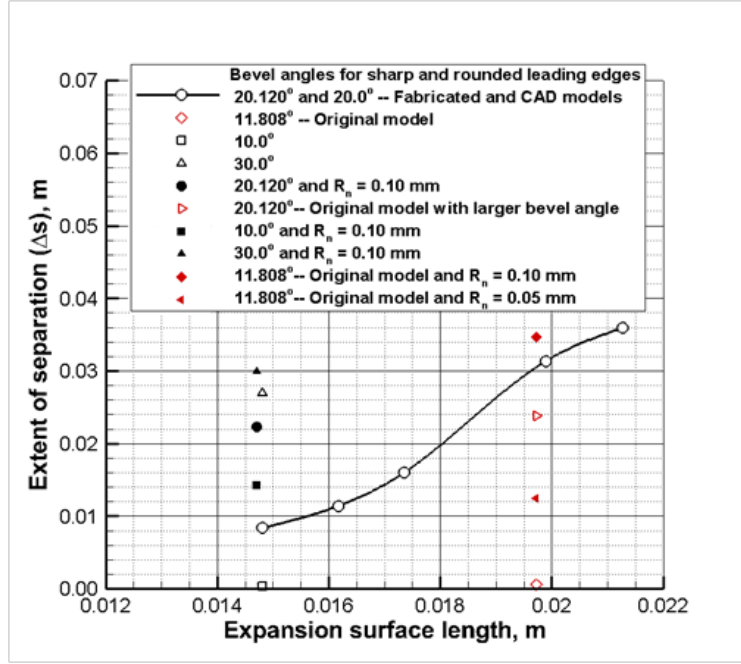


FIGURE 5. Impact of test model configuration on separation size

The solid line connecting the circle symbols in Fig. 5 shows the general trend of increasing separation size with increasing expansion surface length for a 20° bevel angle and a sharp leading edge. This trend is to be expected and is consistent with results from other geometries in which a larger Reynolds number leads to a larger laminar separation. The trends with radius and bevel angle are the same for both expansion surface lengths, only the differences are more apparent for the longer expansion surface length.

The majority of the parametric study was performed at one of two expansion surface lengths, around 0.01475 m and 0.01975 m. The two cases with the smallest (effectively zero) separation extent are sharp with the smaller bevel angle of 10°. The tendency is for Δs to increase with both increasing leading edge radius and with increasing bevel angle. The largest values of Δs for both expansion surface lengths correspond to the largest radius leading edges modeled.

Previous studies of bluntness effects on compression corner flows by Townsend [20] and Holden [21] identified the effects of Mach and Reynolds numbers on the size of the separated region. Reference [21] defines a viscous bluntness interaction parameter β , defined as

$$\beta = \frac{\overline{\chi}_\varepsilon}{\kappa_\varepsilon^{2/3}} \quad (5)$$

where $\overline{\chi}_\varepsilon$ is the modified hypersonic viscous interaction parameter

$$\overline{\chi}_\varepsilon = \frac{\gamma - 1}{\gamma + 1} \left[0.664 + 1.73 \left(\frac{h_w}{h_0} \right) \right] \overline{\chi} \quad (6)$$

where h is the specific enthalpy of the flow and $\overline{\chi}$ is expressed in terms of the Chapman-Rubesin parameter and the Reynolds number,

$$\overline{\chi} = M^3 \sqrt{\frac{\rho \mu}{\rho_e \mu_e}} \frac{1}{\text{Re}_x} \quad (7)$$

while κ_ε is expressed in terms of the leading-edge drag coefficient C_D as

$$\kappa_\varepsilon = M^3 C_D \frac{\gamma - 1}{\gamma + 1} (dx) \quad (8)$$

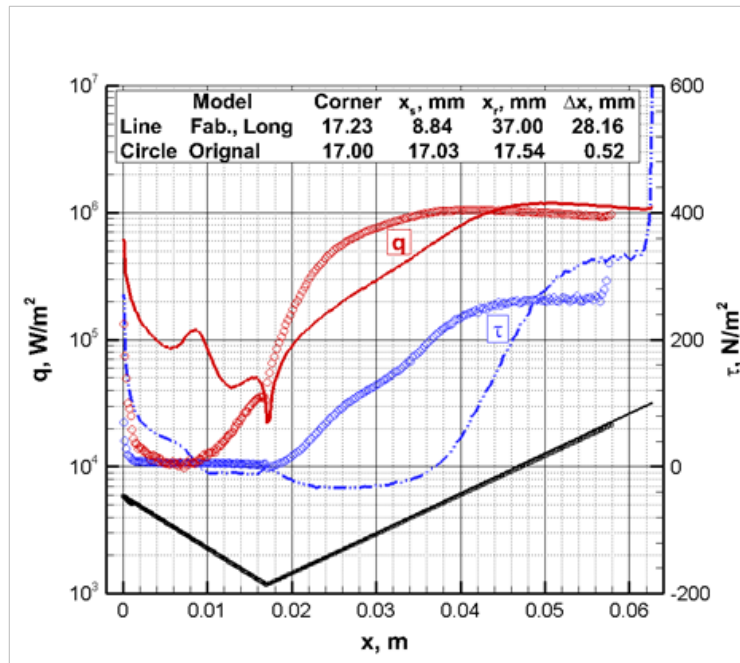


FIGURE 6. Impact of bevel angle on separation size.

where d is the leading-edge diameter. Holden's correlation split the effect of bluntness into two regimes. For $\beta < 0.1$ the bluntness tends to reduce the size of the separated region, while for $\beta > 0.5$, or low bluntness, the bluntness tends to increase the size of the laminar separated region. For the computed case, at $d = 100 \mu\text{m}$, the model falls into the low bluntness domain if the equations shown above are used.

The sensitivity of the size of the separation region to the leading edge radius is a very important result because of its implications for experimental validation of computational results. In the preceding literature there has generally been a lack of specificity in determining the leading-edge radius for nominally sharp leading edge geometries, which this study shows can have a significant effect on the end result of a simulation or experiment. This vagueness is compounded by the differences in assumptions between what an analyst, a computationalist and an experimentalist consider to be a 'sharp' leading edge. For those who treat the flow analytically the sharp leading edge will have zero radius, while for a computational study, the sharpness of the leading edge will be limited by the dimensions of the grid cell nearest to the leading edge, which can be anything from hundreds of nanometers to microns in size. For the experimentalist, the radius of a sharp leading edge is limited by the precision of the cutting machines and methods available. Given the above simulation results, it is not inconceivable that an experimental study of the leading edge separation problem could tacitly assume any of 10, 50 or even $100 \mu\text{m}$ radii to be 'sharp', but would achieve quite different measurements of the size of the separation depending upon which radius was chosen.

The effect of the bevel angle was shown to generate a stronger bow shock and stronger shock/shock interaction above the compression surface. This generates higher pressures on the expansion surface and reduces the effect of rarefaction on the flow. Figure 6 shows the difference for the longer expansion surface results between sharp models having bevel angles of 11.808° (shown as circle symbols) and 20.12° (shown as lines) for both shear stress and wall heat flux distributions. The region over which the shear stress is negative is an indicator of the extent of the separation region. There is a very obvious difference between the shear stress distributions in the two cases. The wedge deflection angle of the flow at these conditions is above the detachment angle at a bevel angle of 20.12° , while the shock wave is predicted to be still attached for a bevel angle of 11.808° . The detached shock provides a high enough pressure to reduce the effect of slip and allow the flow to separate. The effect of the higher bevel angle on the heat flux is to increase the surface heating significantly on the expansion surface and decrease the heating on the initial part of the compression surface, although the peak heating on the compression surface is not significantly different for the two cases.

3. RESONANTLY-ENHANCED SHEARING INTERFEROMETRY

3.1. Facility and Nozzle Flow Conditions

Initially, a contoured nozzle was intended to be used for these experiments, to provide a uniform freestream flow. However, nonuniformities evident in the nozzle exit flow made it necessary to revert to a conical nozzle for these tests, as that nozzle was known from previous studies to produce uniform flow. The uniformity of the nozzle flow was tested using pitot pressure. The nozzle was a 7.5° half-angle conical nozzle having a 12.7 mm throat diameter and a 305-mm exit diameter. Pitot pressure measurements at the beginning of the campaign indicated that at the high-enthalpy condition (referred to as Condition A), the nozzle had an effective expansion angle of 6.7° . At the lower-enthalpy condition, the pitot pressure indicated an effective nozzle divergence angle of 6.9° [22]. The average reservoir and freestream flow conditions are presented in Tab. 1. The nozzle reservoir temperature and enthalpy are calculated assuming chemical equilibrium and isentropic expansion from the reflected shock pressure to the measured nozzle reservoir pressure. The freestream conditions are calculated using the thermal and chemical nonequilibrium one-dimensional flow solver STUBE. This code has been shown to predict nozzle exit temperatures and velocities that are consistent with measurements in these facilities [19].

TABLE 1. Shock tunnel flow conditions

| Condition | | A | E |
|------------------------|------------------------------------|--------|--------|
| enthalpy | H_o [MJ/kg] | 13.5 | 3.8 |
| reservoir pressure | P_{res} [MPa] | 11.1 | 11.5 |
| reservoir temperature | T_{res} [K] | 6920 | 3050 |
| freestream pressure | P_∞ [kPa] | 0.38 | 0.29 |
| freestream temperature | T_∞ [K] | 590 | 165 |
| freestream density | ρ_∞ [kg/m ³] | 0.0020 | 0.0060 |
| freestream velocity | u_∞ [m/s] | 4550 | 2500 |

Figure 7 shows the nozzle reservoir traces for Conditions A and E, each averaged over 10 tunnel runs during the campaign. The averaging helps to remove the noise from the transducers and the effect of the run-to-run variations in pressure. While the plateau pressure is comparable for the two conditions, it is clear that Condition E maintains a steady pressure for at least twice as long as Condition A, which is consistent with the difference in total enthalpy between the two conditions. It is therefore expected that the flow will be steadier for longer at Condition E. There is, however, a period of around 200–250 microseconds at Condition A where the nozzle reservoir pressure is nominally steady.

3.2. Experiment Models

Because these experiments are intended to be used to compare with computational work, and because the computations outlined in Sec. 2 showed strong sensitivity to leading edge radius in the separated flowfield, the experimental model dimensions and angles needed to be carefully quantified. As mentioned previously, the model used for these measurements was designed so that both the leading edge radius and the bevel angle of the model could be varied. For these experiments, nominal leading-edge radii of 10, 100 and 200 μm were used. Bevel angles of 10 and 20° were investigated. The model geometry is shown schematically in Fig. 8. As the diagram indicates, the leading-edge components were replaceable, both to allow for the testing of these different radii and included angles, and to permit the leading edge to be replaced in the event of damage from steel diaphragm fragments impacting the leading edge of the model. While the flow generally will contain some fine particulates, mostly consisting of carbon from the piston rings, grease and the mylar diaphragm at the throat of the nozzle, and steel from the diaphragm that separates the shock tube from the compression tube, there are occasions where steel fragments of sizes between 1 and 3 mm can impinge on the model. During the campaign, the model was regularly inspected and the leading edge radius re-measured using a traveling microscope. Unless one of the larger steel fragments hit the leading edge, causing localized damage, the radius of the leading edge was not measurably affected by abrasion from the small-scale particulates in the flow. The width of the model was 220 mm, providing an aspect ratio of width to expansion-surface length of 11 to 1. This should

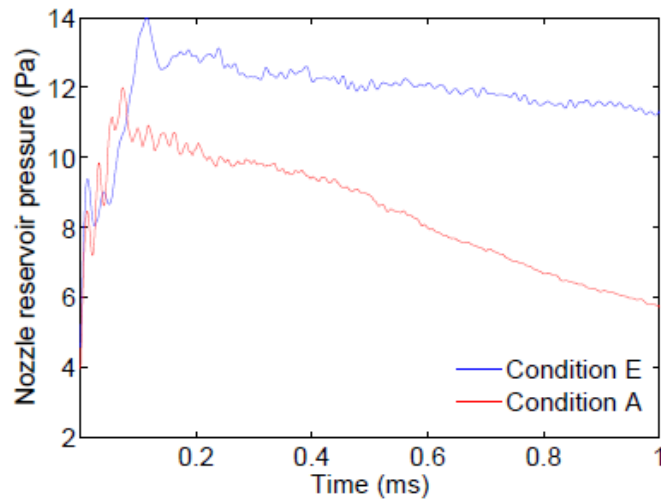


FIGURE 7. Averaged nozzle reservoir traces for Conditions A and E.

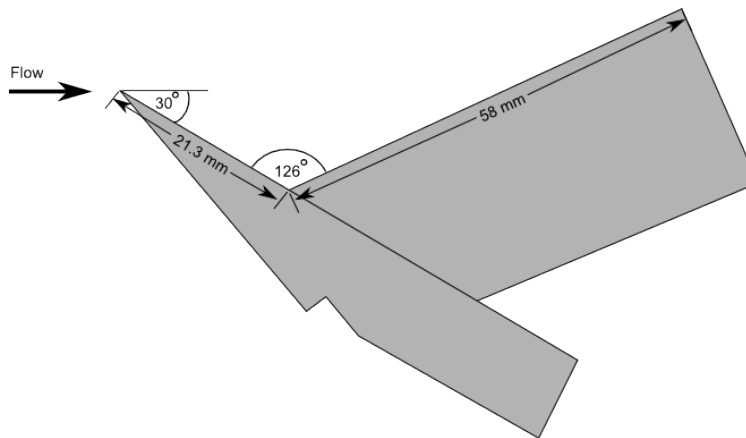


FIGURE 8. CAD image of the experimental model

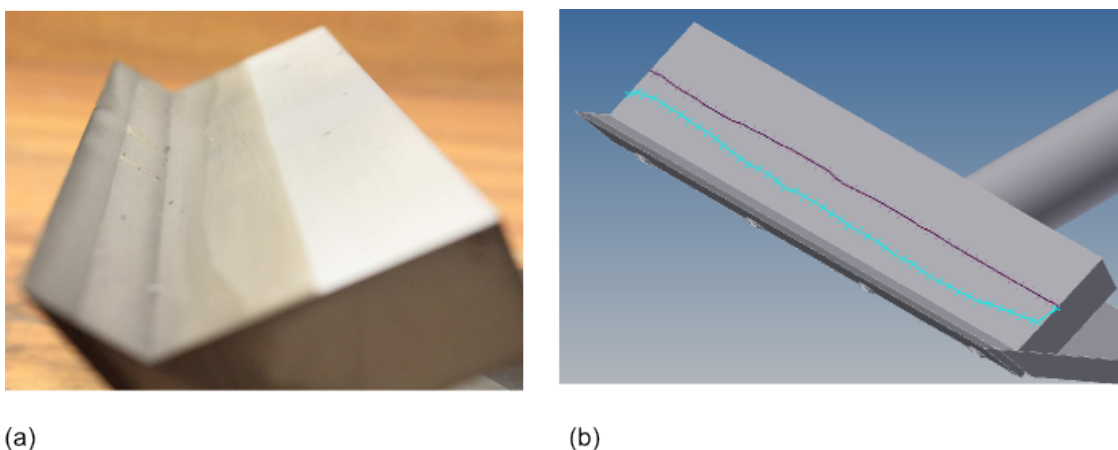
be sufficient to ensure that the flow is two-dimensional. As the nozzle exit diameter is 305 mm, the model should be inside the core flow.

The leading edge portions of the model were fabricated using a wire-cut electric discharge machining method, which limited the minimum leading-edge radius to around $10\text{ }\mu\text{m}$. The models were produced in a single long piece and then cut into multiple sections to provide a number of spares in case of damage to the leading edge. Each of the model characteristic lengths and angles was measured for all of the models, using either a calibrated high-resolution CCD camera image or a traveling microscope, and the results of these measurements are summarized in Tab. 2.

In addition to measuring the model characteristic dimensions and angles, care was taken to determine the precise distance between the leading edge of the model and the exit of the conical nozzle. This is important to determine because the shock tunnel interfaces with the test section using a sliding o-ring adjustment, which allows the nozzle to move away from the test section as the tunnel recoils during a facility run. The tunnel recoils by around 30 mm during the test. As this process is dynamic, and occurs over tens of milliseconds, the position of the nozzle exit relative to the leading edge needed to be monitored throughout the tunnel run. To determine this distance, and its variation from one facility run to the next, the region between the leading edge and the nozzle exit was imaged throughout the facility run

TABLE 2. Average measured parameters for machined model

| | | Average | Standard deviation | Unit |
|--------------------------|-------------------|---------|--------------------|---------------|
| Expansion surface length | 10 μm | 19.56 | 0.18 | mm |
| | 100 μm | 18.55 | 0.05 | mm |
| | 200 μm | 17.50 | 0.03 | mm |
| Compression surface | | 50.01 | 0.02 | mm |
| LE radius | sharp | <10 | — | μm |
| | 100 μm | 0.11 | 0.01 | μm |
| | 200 μm | 0.24 | 0.02 | μm |
| Bevel angle | 10 $^\circ$ | 10.02 | 0.04 | $^\circ$ |
| | 20 $^\circ$ | 20.02 | 0.05 | $^\circ$ |
| Compression corner angle | | 125.09 | 0.10 | $^\circ$ |

**FIGURE 9.** (a) Photograph and (b) digitization of the reattachment and recompression lines for the separation vortex

over ten runs, using the Shimadzu HPV1 high-speed camera, with each pixel resolving a distance of 0.22 mm. In the middle of the nominal test time for Condition A, the distance from the nozzle exit to the leading edge of the model was 16.2 ± 0.7 mm.

After the model had been in the tunnel for a number of facility runs performing the visualizations, the fine dust in the tunnel flow would make patterns on the model surface that clearly show the points of reattachment and recompression on the compression surface of the model. This process is analogous to oil flow visualization that is often used in lower-speed separated flow investigations to provide some idea of the two-dimensionality of the flow. While care must be exercised in interpreting these data, because the pattern is the result of the effect on the dust pattern over a large number of runs, and over the entire test time rather than just the steady-flow test time, the image provides a good indication of the overall degree of two-dimensionality within the separated flow. The results of this visualization after a campaign of facility runs at Condition A is shown in Fig. 9. Fig. 9(a) shows a photograph of the pattern, while Fig. 9(b) shows a digitization of the dust pattern on a CAD model. There is a rapid increase in the size of the vortex near the edges of the model, caused by the interaction of the vortex formed at the corner of the leading edge and the spillage of flow around the sides on the model. The separation region does appear to be uniform in extent over the central two-thirds of the model span.

3.3. RESI Optical System

The RESI technique is described in detail in Hruschka et al. [7], and the details of the optical arrangement are outlined in that paper. In this report, we used the same arrangement, shown in Fig. 10. Two different laser sources were used: a 500 mW Sony SLD133V multi-mode diode laser operating near 670 nm and a 180 mW Photodigm Mercury

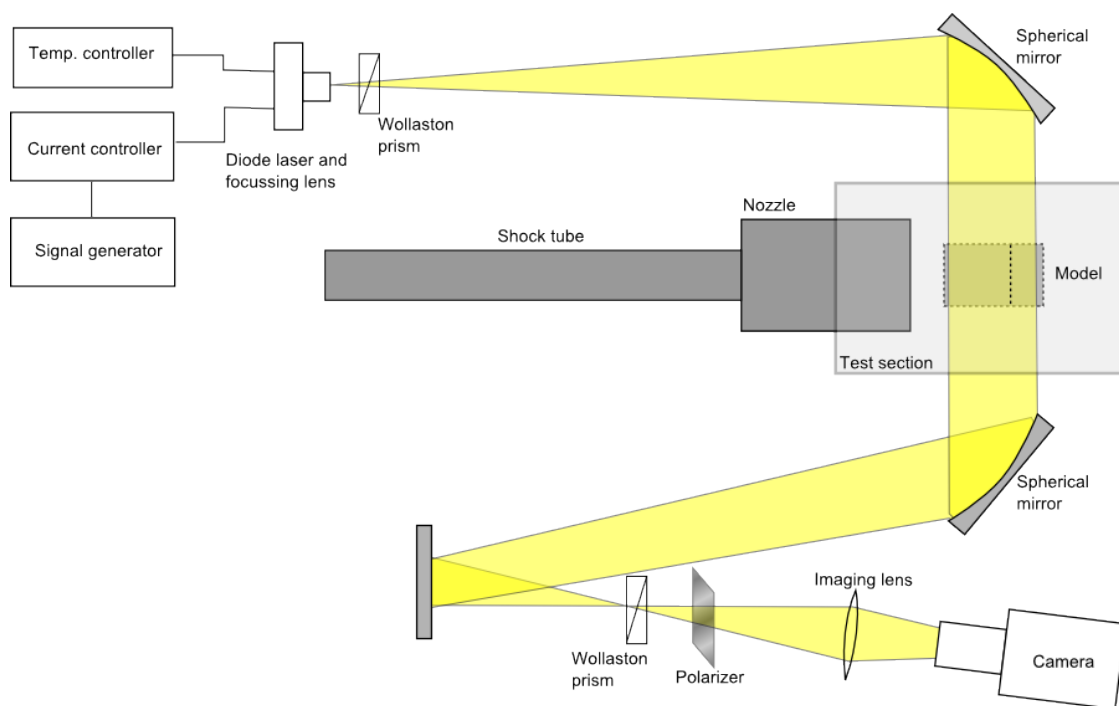


FIGURE 10. RESI optical system

DFB laser operating near the rubidium *D2* lines at 780 nm. The imaging was performed using a Shimadzu HPV1 high-frame-rate monochrome CCD camera. The polarization plane of the Wollaston prisms was set at 45 degrees to the horizontal, to capture components of density gradient in both horizontal and vertical directions. The multi-mode laser was detuned from the line-center of the Li *D2* line by 100 pm, which was found to provide a good compromise between low laser attenuation and resonant refractivity enhancement. The HPV1 camera can acquire up to 1 million frames per second, and a maximum of 100 frames, with a spatial resolution of 312×260 pixels. The images presented in this study were acquired at a rate of 500 000 frames per second, which is sufficient to capture 200 microseconds of flow time. The portion of the flow captured by the camera was determined by delaying the acquisition time of the camera relative to the nozzle reservoir pressure trace registering the shock reflection at the end of the shock tube. The flow imaging time was chosen to cover the steady flow time of the facility.

The main purpose of the study presented here were to investigate the effects of bevel angle and leading edge radius on the separated region. An additional goal was to investigate different variants of the RESI technique, to determine whether better quality images could be obtained by using a salt solution rather than a metal foil to seed the flow, or by using the single-mode laser rather than the multi-mode laser that had been used for the Lithium results. This was important, because the degree of heating, and therefore the achievable seeding level, is lower for the leading-edge separation geometry than it was for the work presented on bluff body wakes in Hruschka et al.'s work. This causes a penalty in the degree of refractivity achievable at the same freestream conditions.

Using the salt solution provides two main potential advantages over the foil: a more uniform seeding distribution, as the liquid RbCl or LiCl solution is much easier to apply evenly to the end wall of the shock tube than the metal Li foil. Previous investigations using metal foil seeding have shown striations in the freestream flow, and these striations may have been a result of the difficulty in achieving uniform seeding in the flow. It is also considerably safer and easier to work the salts of Rb and Li with than the metallic lithium. Metallic Rb was considered too dangerous to use and too easily oxidized for this application. Using the Li or Rb salt also allows very fine control over the seeding of the atomic species into the flow, by controlling the concentration of the solution. The most significant potential disadvantage of salt-based seeding is that the ionic bond in the chloride salts require more energy to break, and thus one would expect a lower seeding concentration of atomic Li in the freestream flow for the salt than for the metal.

Using the single-mode Mercury laser at 780 nm provides the possibility of greater control over the degree of resonant

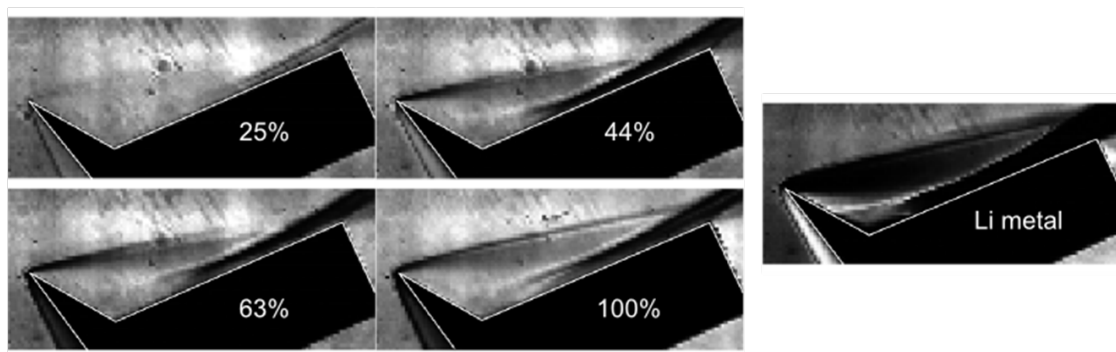


FIGURE 11. Comparison of Li salt at 4 different concentrations and Li metal seeding

refractivity enhancement in the flowfield, and the compromise between enhanced refractivity and laser light extinction. A similar study was attempted by Hruschka [refHruschka2010Optical] using a 10 mW Fabry-Perot laser operating near the Li D lines, but the power of the laser was insufficient to allow good visualizations to be obtained. The Mercury laser, although having a lower overall power at 180 mW than the 500 mW Sony diode, has a higher spectral irradiance because of the much narrower linewidth. In addition, as mentioned earlier, the higher oscillator strength of the Rb lines can also assist in increasing the refractivity enhancement for these flows.

3.4. RESI Results

3.4.1. Variations on the Visualization Technique

The comparison between using lithium chloride salt and lithium metal as a seed for the leading-edge separation at Condition A is shown in Fig. 11. Each of the images was obtained at 500 kframes per second using the Shimadzu HPV1 camera. The first four images are stills from the middle of the steady flow time, each obtained with a different concentration of lithium chloride solution. The percentages shown in the images indicate the percentages of a saturated solution of lithium chloride used to coat the shock tube end wall before the tunnel run. Knowing the exact concentration effect is difficult, however, as there is no guarantee that there will not be an accumulation of unevaporated salt building up from previous facility runs, and this is not accounted for in the percentages. Nevertheless, it is clear from Fig. 11 that the degree of refractivity enhancement, and the amount of absorption in the hotter areas of the flowfield like the forebody shock layer and the post-recompression-shock regions of the flow, both increase as the concentration increases.

Although the salt solution seeding can be seen to enhance the refractivity in a way that increases as the concentration of the salt increases, the degree of enhancement is still not sufficient to allow the separated shear layer to be visualized prior to the initial stages of the reattachment process. It is therefore extremely difficult to determine the separation location for the flow. In contrast, the rightmost image in Fig. [reffig:SaltMetalLi] was obtained using metal foil placed at the end of the shock tube as the seed source for the visualization. It is very clear that the degree of both absorption and resonant refractivity enhancement is much higher when the metallic foil seeding is used. The main reason for this difference is the high dissociation energy of LiCl, releasing only a small quantity of atomic Li into the flow, relative to the metallic source. The image obtained using the metal foil clearly shows the lip shock as a horizontal lighter line near the point of separation, and the location from which the flow separates from the expansion surface. The amount of absorption is also clearly greater for the case of metal foil seeding. There is also some evidence of emission from the shock layer below the expansion surface for the metal foil seeding case.

It was noted that there was less striation in the freestream flow for the salt seeding case than for metal foil seeding. This may either be due to the salt solution providing intrinsically more uniform flow seeding than the foil, but it is also possible that the lower sensitivity of the system makes the background appear more uniform.

The single-mode laser was used with RbCl and was imaged with a Phantom high-speed camera at a much lower speed of 20 kframes per second than obtained with the HPV1 camera for the LiCl case. For these experiments, a

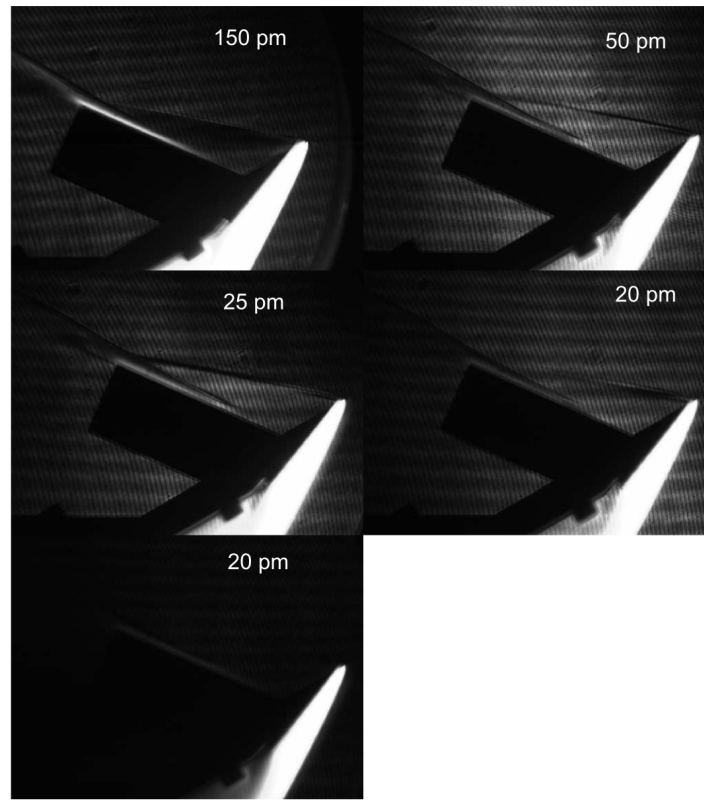


FIGURE 12. Effect of detuning on Rb salt signal

saturated RbCl solution was used for seeding the flow. Fig. 12 summarizes the effect of detuning on the visualizations performed using the single-mode laser and RbCl seeding.

The spatial resolution of the Phantom camera is better than that of the Shimadzu HPV1, but there is a glass plate placed directly in front of the Phantom's CCD chip that produces a strong interference pattern in the background that is not apparent on the HPV1 images. These can be clearly seen as the horizontal band pattern in the images. Because the exposure time is also much greater for the phantom camera, the luminosity on the compression surface is much greater than for the HPV1 camera. Each image in Fig. 12 is obtained at a different detuning from line center, with the detuning shown for each image, in terms of the number of picometers from the line center. Although the reattachment shock and the expansion around the surface are apparent, there is very little resonant enhancement in these images. Also, the results seemed to be inconsistent regarding how the degree of resonance enhancement varies with detuning. One would expect both absorption and refractivity enhancement to increase as the detuning was reduced and the laser emission wavelength brought closer to the line center. However, the furthest detuned image at the top left appears to have more resonant enhancement than the others. At a detuning of 20 pm there are two images provided. One shows significant absorption compared to the other but neither of them show significant resonant enhancement. Because of this inconsistency in results, and the background intensity modulation superimposed on the images, it was decided to discontinue use of both the lower-speed Phantom camera and the single-mode laser. The sensitivity of the single-mode laser system to the level of seeding and the degree of wavelength detuning, plus possibility that the level of seeding can change measurably from one tunnel run to the next means that it would be difficult to achieve consistent quality visualization using this laser. The wide emission range of the multimode Sony laser makes the visualization technique much more repeatable and robust than the single-mode system.

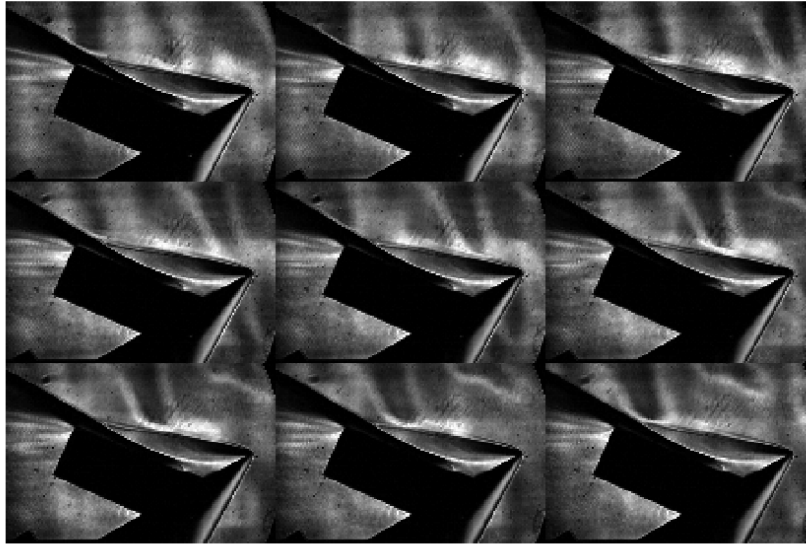


FIGURE 13. Nine consecutive images from steady flow time, each $2\mu\text{s}$ apart.

3.4.2. Steady Flow Time

The continuous laser source and the high-speed camera allow very short times between RESI image acquisitions, so it is possible to qualitatively determine whether the flow reaches a steady state by investigating the range of images for which the separated flow maintains a consistent shape. During the time history of a tunnel run with the leading-edge model configuration, the separated flow tends to increase in size, reach a steady state for some number of acquisitions and then increase in size and become more diffuse. Determining the steady flow time is particularly important at the high-total-enthalpy Condition A, where the duration of the flow is very short. The unsteady DSMC simulations of the flow indicate that at Condition A, the establishment time for the separated flow is of the same order as the available tunnel time.

Figure 13 shows a sequence of 9 consecutive images obtained with a $2\mu\text{s}$ time difference between frames for the flow around a model having a $10\mu\text{m}$ leading edge radius and 20° bevel angle. The size of the separated region remained approximately constant over that time period. Also apparent in the image are the vertical striations in the freestream that were mentioned previously. These are particularly apparent when the metal foil seeding method is used, as was the case in this image. The striations can be seen moving from the right to the left of the image during this image sequence, and provide a measurement of the freestream flow speed that is consistent with predictions from the STUBE code.

3.4.3. Effects of Bluntness and Bevel Angle

The main visualization campaign in this report involved measurements of the effects of leading edge radius and bevel angle on the size of the recirculating region. As described in Sec. 2, both of these parameters were predicted to have a strong effect on the size of the separated region. The two bevel angles showed the difference between the separated regions behind detached and attached shocks, while the different radii showed the effect of a small degree of blunting on the flow field, due to changing the degree of slip along the expansion surface. The computations indicated a peak density-based local Knudsen number in excess of five for the sharp model, indicating significant slip should

TABLE 3. Effect of bluntness and bevel angle on averaged separated flow properties.

| Bevel angle ($^{\circ}$) | Leading edge radius (μm) | Separation distance AS (mm) | Reattachment distance BC (mm) |
|----------------------------|---------------------------------------|-------------------------------|---------------------------------|
| 20 | 10 | 2.1 ± 0.4 | 13.2 ± 2.1 |
| 10 | 10 | 5.8 | 9.5 |
| 10 | 100 | 4.4 | 12.6 |
| 10 | 200 | 3.0 | 16.7 |

occur at these conditions.

The initial set of experiments were performed to compare bevel angles of 10 and 20° for the sharpest (10 μm) leading edge. A second set of experiments was performed using the 10° bevel angle, but with more rounded leading edges having radii of 100 and 200 μm . The findings of the study are summarized in Tab 3 while Fig. 14 shows representative images for each of the configurations studied. The distances presented in Tab. 3 indicate the distance along the expansion surface from the leading edge to the separation point, and the distance along the compression surface from the vertex of the ‘tick’ to the reattachment position.

The most images obtained for any condition was 13 for the 20°, 10 μm case, 7 of which were used with the metal foil seeding. These 7 runs were used to determine the standard deviations presented in Tab. 3. The separation and reattachment distances outlined in the table were measured on the average of the images for the steady flow duration of each tunnel run, to make the location of these two points as clear as possible. The uncertainties show that the reattachment point was a lot more difficult to determine than the separation location, which was usually fairly clear in the images, although on occasion the expansion was thick enough to make it difficult to pinpoint the exact separation point. The merging of the thick recompression shock wave with the reattaching boundary layer, compounded with the variability in the degree of resonant enhancement of refractivity from one facility run to the next, often made it difficult to determine the location of the reattachment point, which explains the larger degree of uncertainty in the position of the reattachment than for the separation location.

A number of trends are apparent in Tab. 3. When comparing the sharp leading edge case between the two bevel angles, there is a clear increase in the distance from the leading edge to the point of separation and a decrease in the distance from the vertex to reattachment as the bevel angle is reduced from 20 to 10°. This indicates a reduction in the size of the separation, which is seen by comparing Fig. 14 (a) and (b). The reduction in the size of the separated region is measurable and statistically significant, but not nearly as dramatic as that predicted in the computational study. Although the lower flow speed in the computations compared with the experiment means that care must be exercised when comparing the two cases, the lower speed for the computations should produce less velocity slip at the surface and therefore a larger separated region in the calculated flowfield. One possible reason for the difference in scale between the reduction in separation size predicted in the DSMC and that measured in the experiment is that, in the experiment, the shock wave at the leading edge appears to be detached in the 10° bevel angle case. The DSMC predicts that the flow should be attached at these conditions, but even in this sharpest angle case, there looks to be a finite distance between the shock wave and the leading edge (emphasized with a white line outlining the model in Fig. 14). If the shock was still detached even for the sharpest leading edge and the smallest bevel angle, this would explain the increased size of the separated region, as the slip on the expansion surface would be reduced. The deflection angle for the 10° bevel angle is 40°, which should remain attached for flows where the Mach number exceeds 5, as should be the case here.

Comparing the effect of bluntness on the 10° bevel angle in Tab. 3 shows a measurable trend in decreasing distance to separation and increasing distance from the vertex to the reattachment point as the radius of the leading edge is increased. The 200 μm case showed more variability in the size of the separation region from one tunnel run to the next, over the four tunnel runs, than the smaller diameters. However, the trend is noticeable, and can be seen in comparing the images from Fig. 14. This trend is consistent with what is predicted by the DSMC simulations. Looking at the shock layer on the lower surface in Figs. 14 (c) and (d), there is a normal portion of the shock wave, caused by the lower support on the model. This was seen to move towards the tip in some of the images, but was not considered to be a large enough effect for upstream influence to affect the flow around the corner.

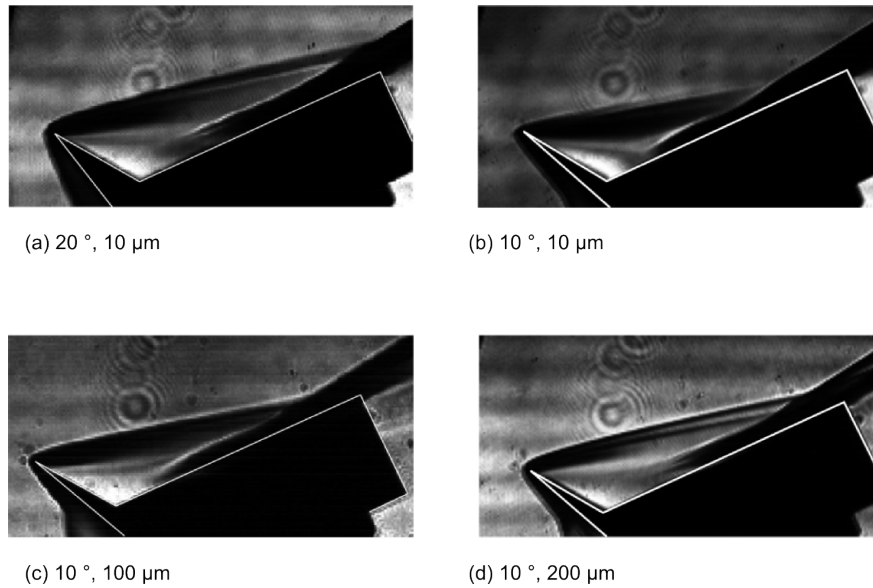


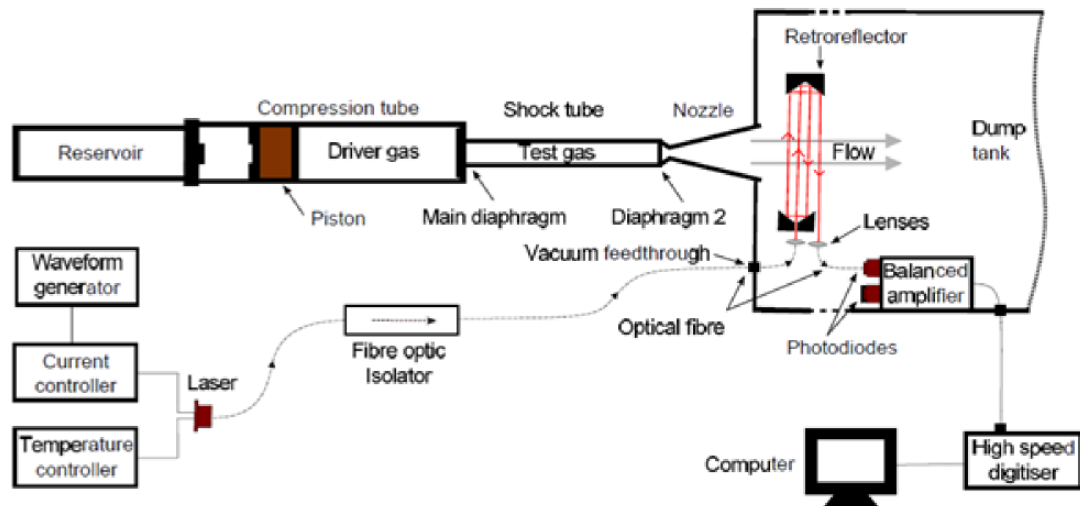
FIGURE 14. Effect of leading edge bluntness and bevel angle on separated flow region

4. TIME-RESOLVED NOZZLE-EXIT TEMPERATURE MEASUREMENTS

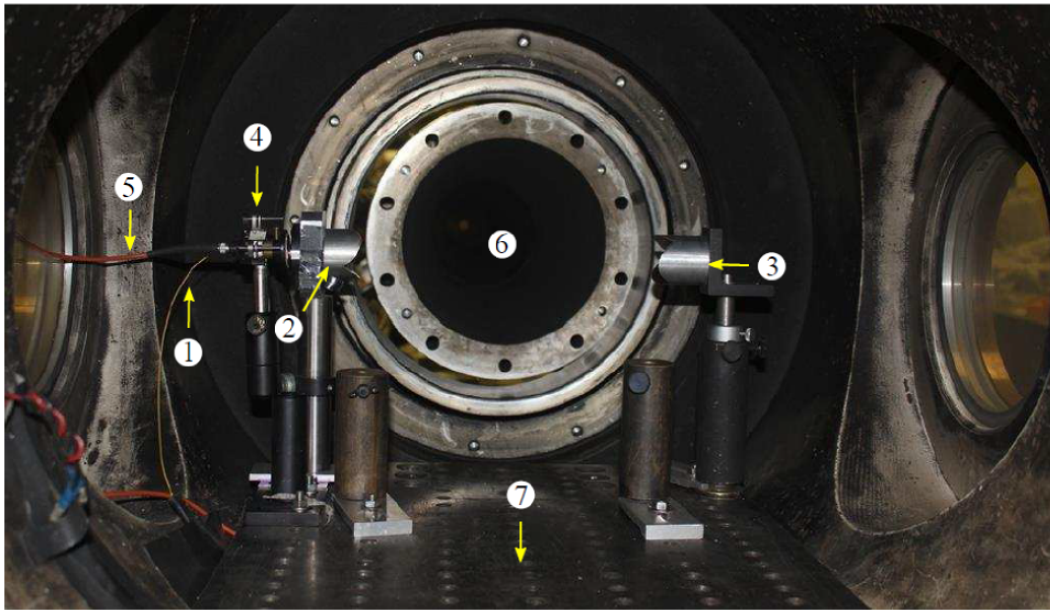
Because shock tunnels are, by their nature, impulse facilities, it is important to quantify the temporal variations in their flow conditions. It is important to be able to quantify how steady the flow is, in order to determine whether the computational assumption of steady flow is a good one, or whether an unsteady simulation of the flow field is required. It can be very difficult to determine at what time the test gas from an experimental facility has been contaminated by the driver gas. These considerations are particularly important when a short-duration flow is being used to investigate a flow with a relatively large vortical region, as is the case for this study. These viscosity-dominated flows require some time to establish the flow, and if the uncontaminated facility time is shorter than the required establishment time, then the experiments will be compromised. Previous theoretical [23] and computational [24] studies have investigated the processes by which driver gas can prematurely contaminate the test gas of a facility. Experimentally, determining whether premature contamination has occurred is very challenging, because the typical pitot or static pressure measurements, or heat flux measurements, are not sensitive to the presence of driver gas. To address this problem, we developed a technique for making time-resolved temperature measurements at the nozzle exit while the visualization experiments are being performed. The temperature of the test and driver gases are different, and so temperature can be used as a sensitive proxy for driver gas contamination. Because of space limitations, we will only briefly describe those aspects of the temperature measurements that are relevant to this study, but much more detail on the design of the system can be found in Krishna's PhD thesis [22].

Tunable diode laser absorption spectroscopy [25] is a technique that has proved very useful for making measurements in high-enthalpy facilities. For these measurements we have chosen to measure the temperature of ambient water in the room air that was used for these experiments. The technique will also work when dry air is used, because there is some water produced from the outgassing of the metals in the tube walls, but the signal is much stronger when room air is used. Absorption of water vapor near 7180 cm^{-1} was used, as the transition parameters are well known and the absorption is relatively strong over a range of temperatures that covers both Condition A and the lower-enthalpy Condition E [22].

The optical arrangement of the measurement system is shown in Fig. 15(a), while Fig. 15(b) shows the arrangement at the exit of the facility nozzle. The system is similar to one that was successfully used to measure oxygen absorption in a scramjet flight test [26], incorporating a pair of offset corner cube retroreflectors to increase the beam path. It should be noted that when this configuration is used, and the retroreflectors are aligned with a component of the direction vector connecting them in the direction of the flow, the sensor can be made sensitive to the freestream velocity. Because we wanted to perform the temperature measurements simultaneously with the RESI visualizations,



(a)



(b)

FIGURE 15. (a) Schematic of the TDLAS system in the shock tunnel, (b) Image of the system in the tunnel: 1. Pitch fiber, 2,3. Retroreflector, 4. Transmission optics, 5. Collection optics, 6. Nozzle, 7. Optical breadboard.

we kept the beam perpendicular to the nozzle exit, and so did not measure flow speed. The transmission and collection optics were located inside the test section, and the light transported to the amplifier and the data acquisition system using a multi-mode optical fiber.

The light source that was used for this system was a Vertilas single-mode vertical-cavity surface emitting laser (VCSEL). These are small solid-state lasers that can be current-scanned very rapidly over a wavelength range of about 1 nm. This allowed us to scan over four transitions in the $v_1 + v_3$ band of water vapor using a single diode laser, ensuring that the system was kept as simple in design as possible. The temperature of the diode was kept stable, while a function generator was used to modulate the current (and therefore the wavelength) of the laser. Detection

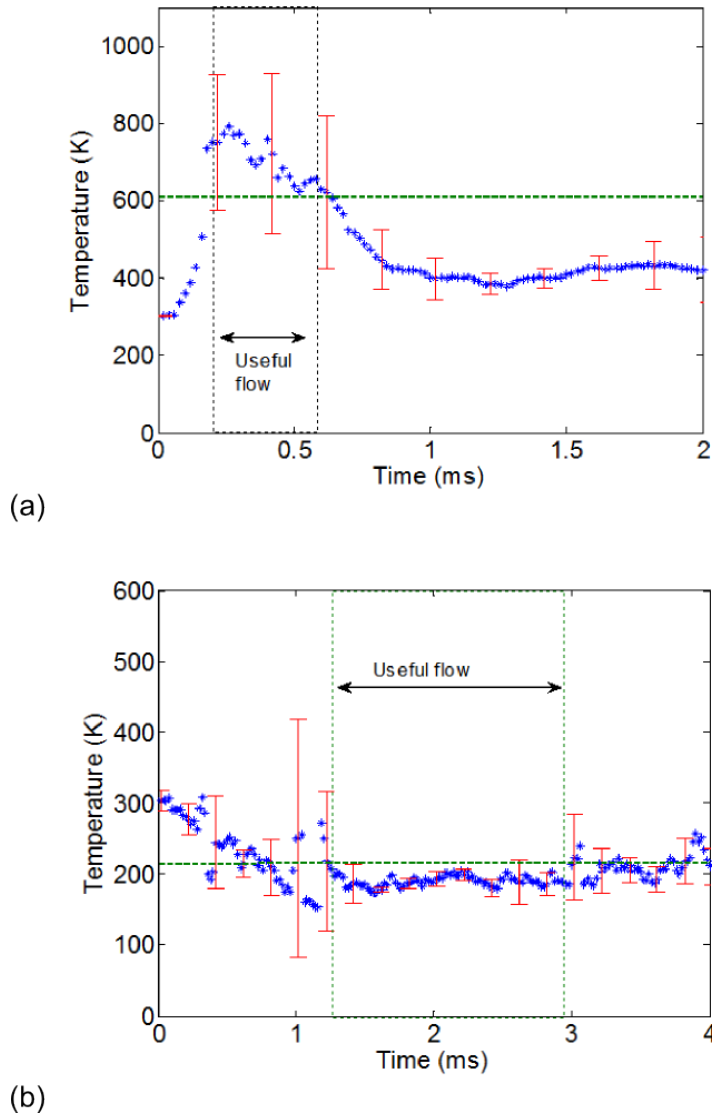


FIGURE 16. Temperature histories for (a) Condition A and (b) a lower-enthalpy Condition E

was performed using a difference amplifier, which was chosen as a good compromise between requirements for speed and precision. Data from the detector was sampled using a 50 MSPS, 16-bit, 2-channel data acquisition system. The differential amplifier removes the amplitude modulation of the signal caused by the current-scanning, allowing more of the analog-to-digital convertor's dynamic range to be used to capture the weak signal than if direct absorption were used.

Once acquired, absorption and reference spectra were obtained and spectrally calibrated using a thick glass etalon. used to determine the absorbance signal. The nonuniform background is fitted and subtracted from the spectrum to produce a zero-offset spectrum. The absorbance signal is integrated over two spectral features, and the ratio of the two integrated absorbances is compared against equivalent ratios obtained by simulating the absorption spectra over a range of temperatures. The fitted temperature is the one that provides the best fit to the ratio. The simulation was performed using the GENSPECT code [27] and the HITRAN spectroscopic database [28].

Figure 16 shows the averaged temperature history of the tunnel for (a) Condition A, the flow condition used in these experiments, and (b) Condition E, a condition with a lower total enthalpy of 3.8 MJ/kg. The error bars on the plots

indicate the standard deviation of the measurements from one tunnel run to the next. The green horizontal lines indicate the temperature predicted by the STUBE code at the nozzle exit. The dashed vertical lines indicate the nominal steady test time of the facility. It is clear from the data that while there is a long steady flow time where the temperature is constant at Condition E, at Condition A the temperature is continually decreasing. The shorter test time is to be expected for Condition A, because the number density in the shock tube is lower, and the mass flux through the nozzle significantly higher for Condition A than for Condition E. Both conditions provide measurements during the nominal steady flow time that are in agreement to within uncertainty with the STUBE predictions.

The signal-to-noise ratio at Condition A is approximately 5:1, and the uncertainty due to the measurement technique is of the order of ± 50 K or less. This is significantly smaller than the error bars indicate, particularly for Condition A. This leads to the conclusion that there are large run-to-run variations in the flow from one tunnel run to the next. This also occurs around the 1 ms mark for Condition E, but this is before the test time, while the flow is establishing. At Condition A, the flow establishment is occurring during the test time, leading to a much more variable flow field. The arrival of the driver gas corresponds to the decline in the temperature and begins around 0.6 ms after shock reflection. The 300 μ s test time at Condition A is close to what is required to establish the separated flow, and the visible variation in the visualizations may be partially due to this mixing of the steady flow time with the nozzle establishment process. It is interesting to note that the pressure plateau seen in Fig. 7 is not visible in the temperature distribution, which shows at Condition A that the temperature is continually dropping during the test.

5. CONCLUSIONS

The following conclusions can be drawn from this report:

- Computational modeling of the flowfield around this leading-edge separation geometry indicates that both leading edge radius and forebody bevel angle can have a strong effect on the size of the leading-edge separation vortex. For a sharp leading edge and a small bevel angle, the DSMC simulation predicts nearly no separation at all.
- The experimental visualizations show the same general trends as the computations, but over a much smaller range of separation sizes than the computations indicate. In particular size of the separation region for the sharpest smaller deflection angle is significantly larger than the computations predict. This would indicate that the degree of slip for the experiments is not as great as would be predicted by the code. Measurements of the slip velocity for the angled flat plate case are planned, so that the degree of slip measured in the tunnel can be directly compared against the predictions of the DSMC code.
- The resonantly enhanced shearing interferometry method provides sufficient sensitivity to visualize the separated flow in this leading-edge separation configuration, despite the very low densities in the flowfield and the lack of a strong shock wave upstream of separation. The best system for visualizing the flowfield involved the use of a powerful multi-mode laser with the lithium seeded into the nozzle flow using a metal foil at the shock tube end wall. While the use of salts to seed the RESI visualizations can make the density sensitivity more uniform across the flowfield, and the sensitivity can be finely controlled by varying the salt concentration, it is apparent that the degree of resonant enhancement of the image is significantly less with seeding salt than can be obtained using metallic lithium foil seeding. For this geometry, the refractivity enhancement offered by the salt was not sufficient to clearly see the flow features in the low-density separated region. However, for flowfields like bluff-body wakes, where there is a significant flow stagnation region upstream of the separated flow, the use of the lithium salt seeding method has the potential to provide more uniform seeding and greater sensitivity control, and is a potentially very useful extension of the technique.
- It was found that using a single-mode laser with the Rb D_2 line and RbCl salt seeding did not provide as good a quality of visualization as the broadband laser tuned 100 pm from the Li D_2 line center. Although several laser detunings were investigated, the images were either too dark, because the absorption was too great, or the degree of enhancement was not sufficient to show the flow features. While it is possible that there is a combination of detuning and seeding concentration that might provide a good quality visualization with the single-mode laser, it would not be easy to find, not least because the concentration of the seed species varies from one tunnel run to another. The great benefit of using the multi-mode laser for RESI visualization is that the quality of the visualization is insensitive to the detuning from the transition line center, because the broad wavelength range of the emission means that some portion of the light will be absorbed, some will experience refraction enhancement

without significant absorption and some will not experience enhancement but will propagate through the system to provide background illumination of the image. This ensures that the image is adequately illuminated while still experiencing enhancement of the refractivity.

- In spite of the Rb salt seeding and the narrow linewidth laser not being as effective for the visualization method, the combination of these two elements provides the possibility for quantitative absorption-based temperature measurements in this flowfield. By current-tuning the laser at a rate of 10 kHz across the $D2$ line of Rb, using a very weak salt solution for seeding, it should be possible to obtain images during the steady test time of the facility using the high-speed camera. Each pixel of the image will, over 100 images, have 100 absorption measurements. By fitting a Gaussian curve to this absorption data, the width of the Gaussian can be used to make a translational temperature measurement using the Doppler width of the spectral lines. While not spatially resolved, this method can be used to make accurate temperature measurements during a single tunnel run, provided the flow conditions are sufficiently steady and the level of seeding is uniform.
- We have developed and installed an *in-situ* temperature measurement system based upon tunable diode laser absorption spectroscopy that can measure the freestream temperature at rates of 50 kHz, while the visualization experiments are being performed. This provides very valuable information about the run-to-run variability of the freestream temperature, and provides an indication of the arrival of the driver gas in the test flow. This is particularly important at higher-enthalpy flow conditions like Condition A, where the driver gas contamination can occur earlier than planned in the test gas. The TDLAS measurements showed that the flow at Condition A was much less repeatable than at lower enthalpy conditions, and that the temperature appears to continuously decrease over the duration of the flow, and that the steady flow indicated by the nozzle reservoir pressure trace is not apparent in the nozzle exit temperature history. It may be necessary to simulate the decrease in temperature over time to provide good agreement between computations and experiment, but the on-line temperature measurements at least make this possible. We are also using this new diagnostic to search for a condition with a lower driver gas compression ratio that may provide a flow of the same total enthalpy as Condition A but with a longer steady flow duration.

The main ongoing work for this project involves measurement of quantitative temperature and velocity using planar laser-induced fluorescence of NO. During the funding period an NO PLIF system has been set up, with a high efficiency generation system for 226-nm light and a very highly time-resolved intensified camera system, but these experiments are ongoing. NO rotational temperatures and velocity distributions will be obtained in the presence and absence of the compression surface. In the absence of the surface, the flow will be a flat plate boundary layer with a preceding strong expansion. The visualizations presented in this report, along with the temperature and velocity data without the compression surface will be provided to computational researchers as a means of calibrating their codes to the flowfield, while the rotational temperature and velocity measurements in the presence of the compression step will be saved for a blind test against the codes. Further into the future, under the Australian Research Council Grant facilitated by this project, CARS data for freestream vibrational and rotational temperatures of N_2 and O_2 will be provided to help characterize the freestream and select regions in the 'tick' model leading-edge separated flowfield. Once that is achieved, modellers will have access to important information about the thermal state of a hypersonic nonequilibrium separated flowfield that has previously been unavailable. This should help to significantly reduce the uncertainty in modeling these flows.

6. ANNEX A: OUTPUTS ARISING FROM THE GRANT

- **Papers published in peer-reviewed journals**

Krishna, Y, Kurtz, J and O'Byrne, S (2014) "Baseline Correction for Stray Light In Log-ratio Diode Laser Absorption Measurements", Applied Optics, Vol. 53, Issue 19, pp. 4128-4135.

- **Papers published in peer-reviewed conference proceedings**

Moss, JN, O'Byrne, S, Gai, SL (2014) "Hypersonic Separated Flows about 'Tick' Configurations with Sensitivity to Model Design", proceedings of the 29th Rarefied Gas Dynamics Symposium, Xian, China.

Moss, JN, O'Byrne, S, Deepak, NR and Gai, SL, (2012) "Simulations of Hypersonic, High-Enthalpy Separated Flow over a 'Tick' Configuration", Proceedings of the 28th International Symposium on Rarefied Gas Dynamics, Zaragoza, Spain, 9-13 July.

Khraibut, A, Gai, SL and Neely, A (2015) "Bluntness Effects on Hypersonic Leading Edge Separation," AIAA-2015-0984, 53rd AIAA Aerospace Sciences Meeting, Kissimmee, FL.

- **Papers published in non-peer-reviewed journals and conference proceedings**

- **Conference presentations without papers**

S. O'Byrne, "Laser and Laser Spectroscopy Applied to Hypersonic Flow", Invited presentation, Optical Society of America Light, Energy and the Environment Conference, Canberra, Australia, December 2-5, 2014.

S. O'Byrne, "Laser diagnostics applied to plasmas and hypersonic flows," Invited presentation, EUCASS Aerospace Thematic Workshop, Aussois, France.

T. Kaseman, Y. Krishna, H. Kleine and S. O'Byrne (2014) "Li and Rb near-resonantly enhanced shearing interferometry in a free-piston shock tunnel," Presented at the 29th International Symposium on Rarefied Gas Dynamics, Xi'an, China.

- **Manuscripts submitted but not yet published**

Y. Krishna, S. Sheeche, S. O'Byrne, "Diode Laser Absorption Measurements in the T-ADFA Free-Piston Shock Tunnel" submitted to the 2015 AIAA Aviation Conference, July 2015.

Y. Krishna, "Diode laser spectroscopy for high-enthalpy facility and hypersonic flight characterisation," PhD Thesis, University of New South Wales, Submitted for review September, 2014.

- **List any interactions with industry or with Air Force Research Laboratory scientists or significant collaborations that resulted from this work**

This work has directly led to a large-scale collaborative research effort to compare experimental measurements for this geometry with computational simulations (co-ordinated through the web site www.separatedflows.org) with the following institutions:

NASA Langley Research Center (Dr. J. N. Moss)

University of Minnesota (Prof. G. Candler, Prof. T. Schwartzenuber)

University of Michigan (Prof. Iain Boyd)

University of Illinois at Urbana-Champaign (Prof. D. Levin)

KAIST, South Korea (Dr. C. Park)

National Chiao-Tung University, Taiwan (Prof. J-S Wu)

Taiwan National Space Organization (Dr Y-S Chen)

US Air Force (Dr Jonathan Burt)

The collaboration is funded by an Australian Research Council Discovery Projects grant that extends this project to measurements of vibrational and rotational temperatures of the majority species in the flow.

ACKNOWLEDGMENTS

The computational results presented in this report were computed by Dr J.N. Moss using the DS2V code of Graham Bird. We gratefully acknowledge both contributions to this work.

REFERENCES

1. D. R. Chapman, D. M. Kuehn, and H. K. Larson, Investigation of Separated Flows in Supersonic and Subsonic Streams with Emphasis on the Effect of Transition, Tech. Rep. Technical Report 1356, NACA (1958).
2. H. Babinsky, and J. K. Harvey, *Shock wave-boundary-layer interactions*, vol. 32, Cambridge University Press, 2011.
3. D. Chapman, An analysis of base pressure at supersonic velocities and comparison with experiment, Tech. rep., NACA Report 1051 (1951).
4. J. Moss, S. O'Byrne, N. Deepak, and S. Gai, "Simulations of hypersonic, high-enthalpy separated flow over a 'tick' configuration," in *Proceedings of the 28th International Symposium on Rarefied Gas Dynamics*, AIP Publishing, Zaragoza, Spain, 2012, vol. 1501, pp. 1453–1460.
5. G. V. Candler, I. Nompelis, M.-C. Druguet, M. S. Holden, T. P. Wadhams, I. D. Boyd, and W.-L. Wang, *CFD validation for hypersonic flight: hypersonic double-cone flow simulations*, Defense Technical Information Center, 2006.
6. M. S. Holden, T. P. Wadhams, J. K. Harvey, and G. V. Candler, Comparisons between measurements in regions of laminar shock wave boundary layer interaction in hypersonic flows with Navier-Stokes and DSMC solutions, Tech. rep., DTIC Document (2006).
7. R. Hruschka, S. O'Byrne, and H. H. Kleine, *Applied Optics* **47**, 4352–4360 (2008).
8. W. Merzkirch, *Flow visualization*, Academic Press, 1987.
9. G. Settles, *Schlieren and shadowgraph techniques*, (2001), Springer-Verlag, Berlin, 2001.
10. A. P. Thorne, U. Litzen, and S. Johansson, *Spectrophysics: principles and applications*, Springer-Verlag, 1999.
11. D. A. Leonard, and J. C. Keck, *ARS Journal* **32**, 1112–1114 (1962).
12. G. Blendstrup, D. Bershader, and P. Langhoff, *AIAA Journal* **16**, 1106–1108 (1978).
13. A. Rasheed, K. Fujii, H. Hornung, and J. Hall, "Experimental investigation of the flow over a toroidal aerocapture ballute," in *AIAA Paper 2001-2460*, 2001.
14. A. Bishop, *Spectrally Selective Holographic Interferometry Techniques for Flow Diagnostics*, Ph.D. thesis, University of Queensland, School of Mechanical and Mining Engineering (2001).
15. T. J. McIntyre, A. Bishop, T. Eichmann, and H. Rubinsztein-Dunlop, *Applied Optics* **42**, 4445–4451 (2003).
16. J. Moss, S. O'Byrne, and S. Gai, "Hypersonic separated flows about," in *Proceedings of the 29th International Symposium on Rarefied Gas Dynamics*, AIP Publishing, 2014, vol. 1628, pp. 162–169.
17. G. A. Bird, *Molecular Gas Dynamics and the Direct Simulation of Gas Flows*, Oxford: Clarendon Press, 1994.
18. G. Bird, DS2V (2014), URL <http://gab.com.au/index.html>.
19. R. Hruschka, *Optical studies and simulations of hypervelocity flow fields around blunt bodies*, Ph.D. thesis, University of New South Wales (2010).
20. J. C. Townsend, Effects of leading-edge bluntness and ramp deflection angle on laminar boundary-layer separation in hypersonic flow, Tech. rep., NASA TN D-3290 (1966).
21. M. Holden, *AGARDograph AG-203*, 41–110 (1975).
22. Y. Krishna, *Diode laser spectroscopy for high-enthalpy facility and hypersonic flight characterisation*, Ph.D. thesis, University of New South Wales (2014).
23. H. Mirels, *AIAA Journal* **2**, 84–93 (1964).
24. R. J. Goozee, P. A. Jacobs, and D. R. Buttsworth, *Shock waves* **15**, 165–176 (2006).
25. M. G. Allen, *Measurement Science and Technology* **9**, 545 (1998).
26. J. Kurtz, M. Aizengendler, Y. Krishna, P. Walsh, and S. O'Sbyrne, "Flight test of a rugged scramjet-inlet temperature and velocity sensor," in *AIAA Science and Technology Forum, Kissimee, FL, AIAA- 2015-0110*, 2015.
27. B. M. Quine, and J. R. Drummond, *Journal of Quantitative Spectroscopy and Radiative Transfer* **74**, 147–165 (2002).
28. L. S. Rothman, I. E. Gordon, A. Barbe, D. C. Benner, P. F. Bernath, M. Birk, V. Boudon, L. R. Brown, A. Campargue, J.-P. Champion, et al., *Journal of Quantitative Spectroscopy and Radiative Transfer* **110**, 533–572 (2009).